communications physics

Article

https://doi.org/10.1038/s42005-024-01759-7

# Non-equilibrium excited-state fractionally quantized Hall effects observed via current bias spectroscopy



U. Kushan Wijewardena [1,2,4], Ramesh G. Mani [1,4] ✉, Annika Kriisa [1], Christian Reichl [3] & Werner Wegscheider [3]

Studies of fractional quantum Hall effects (FQHE) across various two-dimensional electronic systems (2DES) have helped to establish the equilibrium FQHE many-body ground states with fractionally charged excitations and composite particles in condensed matter. Then, the question arises whether an FQHE system driven to non-equilibrium can approach a different stationary state from the known equilibrium FQHE states. To investigate this question, we examine FQHE over filling factors, $\nu$, $2 \geq \nu \geq 1$ under non-equilibrium finite bias conditions realized with a supplementary *dc*-current bias, $I_{DC}$, in high mobility GaAs/AlGaAs devices. Here, we show that all observable canonical equilibrium FQHE resistance minima at $|I_{DC}| = 0$ undergo bimodal splitting vs. $I_{DC}$, yielding branch-pairs and diamond shapes in color plots of the diagonal resistance, as canonical FQHE are replaced, with increasing $I_{DC}$, by excited-state fractionally quantized Hall effects at branch intersections. A tunneling model serves to interpret the results.

Fractional quantum Hall effects (FQHE) have introduced quantum fluids with fractionally charged excitations and composite particles into the world of theoretical physics and, more broadly, revolutionized low dimensional quantum condensed matter physics in the modern era[1–19]. To date, FQHEs have been observed in many physical systems, including semiconductor GaAs/AlGaAs heterostructures[5], Si MOSFETs[20,21], AlGaN/GaN heterostructures[22], Ge[23] and InAs[24] quantum wells; in oxides[25,26]; and a number of 2D atomic layer materials[8,9,27–30]. Experimental studies of FQHE mostly examine equilibrium conditions corresponding to nearly zero bias at the several nano-ampere level of ac-excitation of the specimen[6], as theory seeks out the lowest energy or ground state for the equivalent many-body system in the magnetic field[7]. In experiment, however, electronic systems can be driven out of equilibrium with weak photoexcitation[31] or by applying a finite bias, while theoretical numerical studies of finite-sized systems have long indicated the existence of excited states above the FQHE ground states[32]. It is also known that a quantum many-body system driven to non-equilibrium tends to approach a stationary state that is distinct in character from the ground state[33]. Hence, we examine FQHE by experiment over Landau level filling factors, $\nu$, $2 \geq \nu \geq 1$ under non-equilibrium finite bias conditions realized upon applying a supplementary *dc*-current bias, $I_{DC}$, in a magnetotransport experiment in high mobility GaAs/AlGaAs Hall bar devices. Our experiments demonstrate that all observable canonical FQHE incompressible states between $2 \geq \nu \geq 1$ at $|I_{DC}| = 0$ undergo bimodal linear splitting of the resistance minima vs. $I_{DC}$ for $|I_{DC}| > 0$, yielding branch-pairs and diamond-like transport characteristics in the $I_{DC}$ vs. $B$ color plots of the resistance, as the canonical equilibrium FQHE at 4/3, 7/5, 12/9, 5/3, 8/5 etc., are replaced with increasing $I_{DC}$, by non-equilibrium excited-state fractionally quantized Hall effects at the intersection of resistance minima branches originating from different equilibrium FQHE. A qualitative model examining the coincidence between an effective source or drain and mobility gaps in the 2DES reproduces the observed branch-pairs and the diamond-like magnetotransport characteristics and suggests a hybrid origin for the observed non-equilibrium excited-state FQHEs at $|I_{DC}| > 0$.

## Results

FQHE are characterized by vanishing diagonal resistance, $R_{xx}$, and quantized plateaus in the Hall resistance, $R_{xy}$, in a magnetic field, $B$, in a 2DES, at $R_{xy} = h/(p/q)e^2$, where $p/q$ represents rational fractions, with $q$ taking on mostly odd integer values, as $T \rightarrow 0$ K, in the vicinity of fractional filling factors of Landau levels, i.e., $\nu = nh/eB \approx p/q$. Here, $n$ is the carrier density, $h$ is Planck's constant, and $e$ is the electron charge[1–3]. FQHE in the lowest Landau level are often understood in terms of the composite fermion (CF) theory, which indicates that an even number ($2m$) of flux quanta, $\phi_0 = h/e$, bind to each electron to create a composite fermion that experiences a

[1]Department of Physics & Astronomy, Georgia State University, Atlanta, GA, 30303, USA. [2]Georgia College and State University, Milledgeville, GA, 31061, USA. [3]Department of Physics, ETH Zurich, 8093 Zurich, Switzerland. [4]These authors contributed equally: U. Kushan Wijewardena, Ramesh G. Mani.
✉e-mail: mani.rg@gmail.com

reduced effective magnetic field $B^* = B - 2mn\phi_0$, where $m = 1, 2, 3...$, and $n$ is the density of carriers[3]. Thus, for example, with $m = 1$, which corresponds to two flux quanta bound to one electron, the filling factor $\nu = 1/2$ that corresponds to $B^* = 0$, occurs at magnetic field $B = 2n\phi_0$[3,34]. Further, the $\nu = 1/3$ FQHE ($\nu = 1$) at $B^* = +n\phi_0$ ($-n\phi_0$) is viewed as the $\nu = 1$ ($-1$) Integer Quantum Hall Effect (IQHE) state for CF. For $1 \geq \nu \geq 2$, the situation examined here, the CF theory invokes, from symmetry, the rules $\nu = 2 - p/(2p - 1) = 4/3, 7/5, 10/7\ldots$ for $p = 2, 3, 4\ldots$, and $\nu = 2 - p/(2p + 1) = 5/3, 8/5, 11/7, \ldots$ for $p = 1, 2, 3\ldots$, for the FQHE over these $\nu$[3,35]. The Hall resistance trace exhibiting FQHE may also be viewed as a fractal due to the possibility of building up this trace through the iterative application of the same transformations to the Hall resistance and magnetic field axis of a suitable Hall trace template[36].

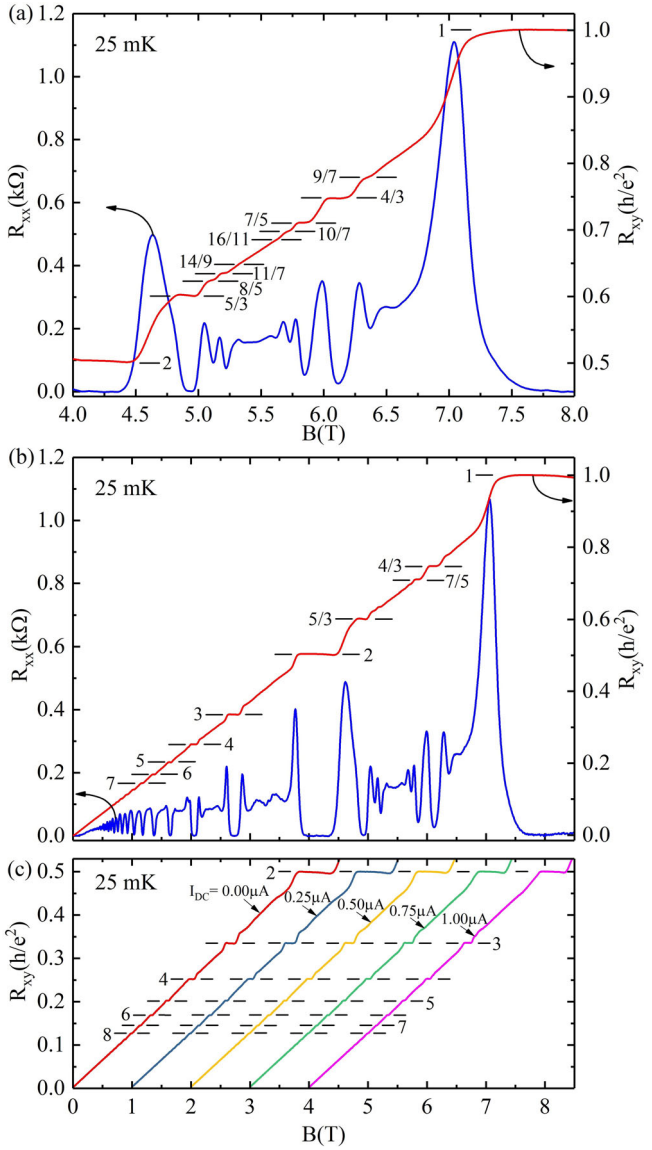


**Fig. 1 | Transport characteristics of a GaAs/AlGaAs heterostructure Hall bar device at T = 25 mK. a** The diagonal ($R_{xx}$) and off-diagonal Hall ($R_{xy}$) resistances are exhibited between $4 \leq B \leq 8$ Tesla, corresponding to the filling factor range $2 \leq \nu \leq 1$, to highlight observable FQHE. **b** $R_{xx}$ and $R_{xy}$ are exhibited for the full range $0 \leq B \leq 8.5$ Tesla. **c** $R_{xy}$ are exhibited for the IQHE regime between $0 \leq B \leq 4.5$ Tesla, for different DC bias currents ($I_{DC}$) between $0 \leq I_{DC} \leq 1$ μA in steps of $\Delta I_{DC} = 0.25$ μA. The traces, which indicate that $I_{DC}$ does not modify observable IQHE (marked by horizontal lines), have been offset along the abscissa by 1 Telsa for the sake of clarity.

Figure 1 establishes the FQHE characteristics observed in the specimens examined here, which are small Hall bars that are much reduced in size in comparison to the up to 5 × 5 mm square-shaped GaAs/AlGaAs devices often examined in the literature[6]. Other studies of similar small samples have been reported elsewhere[37–39]. These previous studies indicate that boundary scattering rather than bulk scattering predominates at low magnetic fields[37] and that there is a size dependence in the tilt-angle-induced crossover between FQHE[39]. Figure 1a shows $R_{xx}$ and $R_{xy}$ vs. $B$ over $2 \geq \nu \geq 1$. Here, FQHE are observable at 9/7, 4/3, 7/5, 10/7 (13/9 is missing), followed by 16/11, on the high $B$ side ($B \geq 5.5$ Tesla) of $\nu = 3/2$, and FQHE are observable at 5/3, 8/5, 11/7 and 14/9 on the low $B$ field side ($B \leq 5.5$ Tesla) of $\nu = 3/2$. Fig. 1b exhibits the full transport characteristics over the $B$-field range $0 \leq B \leq 8.5$ Telsa, which also highlights the typical IQHE features at $B \leq 4.5$ Tesla[40]. Figure 1c exhibits the $R_{xy}$ over the IQHE regime $0 \leq B \leq 4.5$ Tesla now with a supplemental $I_{DC}$ as indicated. These data (Fig. 1c) indicate that the usual IQHE plateaus remain observable and quantized with a concurrent $I_{DC}$ up to $I_{DC} = 1$ μA. These results set the stage for the current bias measurements in the FQHE regime between $2 \geq \nu \geq 1$.

Figure 2 shows line graphs of $R_{xx}$ and $R_{xy}$ for $4 \leq B \leq 8$ Tesla, i.e., $2 \geq \nu \geq 1$, at $I_{DC} = 0.0$, 0.3, and 0.6 μA for a $W = 400$ μm Hall bar. This figure shows, for example, that the 4/3 FQHE $R_{xx}$ minimum disappears by $I_{DC} = 0.3$ μA (Fig. 3b) and turns into a resistance maximum by $I_{DC} = 0.6$ μA (Fig. 3c). Concurrently, the $R_{xy}$ trace also shows the disappearance of the associated FQHE Hall plateau, as other plateaus in the immediate neighborhood, e.g., 17/13 = 1 + 4/13 and 15/11 = 1 + 4/11, become observable.

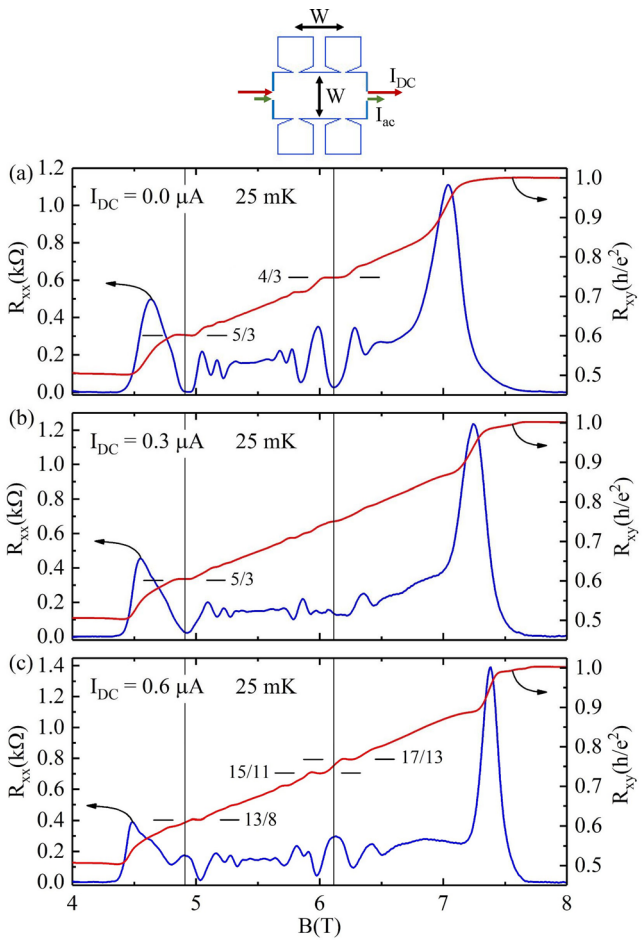


**Fig. 2 | The 4/3 and 5/3 FQHE disappear with increasing $I_{DC}$ at $T = 25$ mK.** A sketch of the Hall bar device section with $W = 400$ μm. $R_{xx}$ and $R_{xy}$ are exhibited vs. the magnetic field $B$ for different $I_{DC}$. Thus, in **a**, $I_{DC} = 0.0$ μA, in **b**, $I_{DC} = 0.3$ μA, and in **c**, $I_{DC} = 0.6$ μA. Note that the 4/3 and the 5/3 FQHE disappear with increasing $I_{DC}$ as additional plateaus appear in the immediate vicinity.

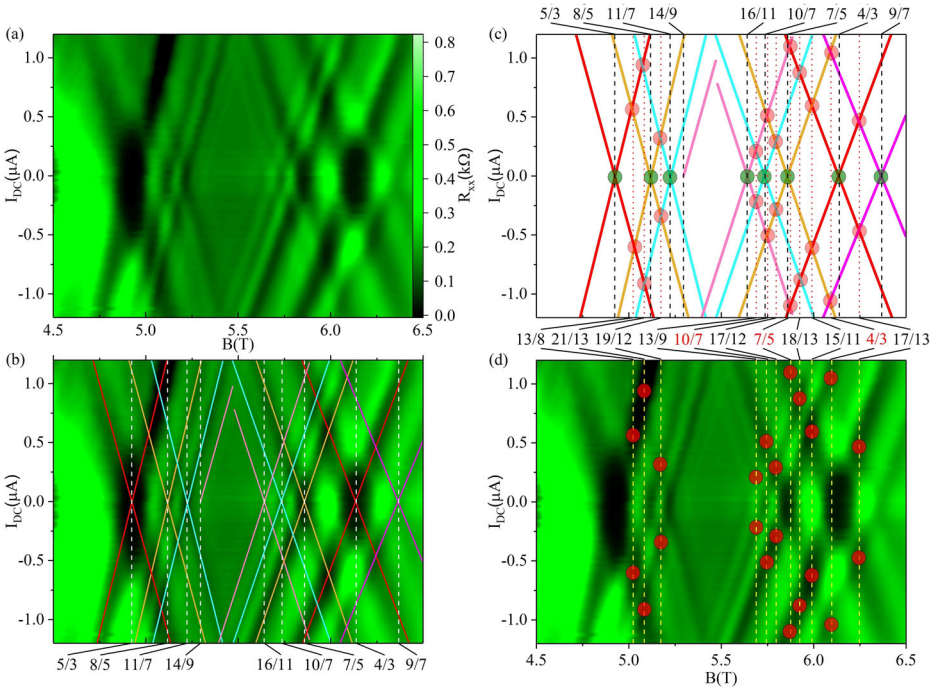


**Fig. 3 | Splitting of equilibrium FQHE states under current bias. a** A color plot of $R_{xx}$ at $T$ = 25 mK vs. the current bias $I_{DC}$ (ordinate) and vs. the magnetic field $B$ (abscissa). The color bar on the right indicates the magnitude of $R_{xx}$. **b** Dashed lines indicate the filling factor, $\nu$ = 5/3, 8/5, 11/7, 14/9, 16/11, 10/7, 7/5, 4/3, and 9/7. Colored solid lines have been overlaid on the color plot in (**a**) to indicate the evolution of the resistance minima with $I_{DC}$. Color code for these lines: Red: 5/3 and 4/3 minima. Gold: 8/5 and 7/5 minima. Light Blue: 11/7 and 10/7 minima. Magenta: 14/9 and 16/11 minima. Violet: 9/7 minimum. **c** This plot shows just the solid line trajectories from plot (**b**), without the color plot. The green points mark equilibrium FQHE. Light-red points mark the intersections of lines originating at different equilibrium FQHE. Fractional filling values assigned to the red dots are given below this panel. The filling factors marked in red are the canonical FQHE filling factors: 4/3, 7/5, and 10/7. **d** Dark red points that mark intersections of lines in (**c**) are overlaid on the data color plot. Red dotted lines in (**c**) and white dashed lines in (**d**) mark the LL filling factor corresponding to the red points, which are indicated between panels (**c**) and (**d**). The experiment suggests non-equilibrium excited-state fractionally quantized Hall effects at these red points.

Similarly, in the neighborhood of the 5/3 FQHE, the 5/3 disappears as 13/8 appears in its vicinity in Fig. 2c with $I_{DC}$ = 0.6 μA.

Figure 3 examines in detail a color plot of $R_{xx}$ vs. $B$ and vs. $I_{DC}$, with $I_{DC}$ taking on both positive and negative values. Figure 3a shows the $R_{xx}$ color plot with the color scale bar on the right. Here, dark or black regions indicate low resistance or conductance, while bright green indicates high resistance or conductance. The features of interest in this plot are the numerous positive-slope and negative-slope dark (low resistance/conductance) diagonal bands; bands that form a sequence of "X"-like and nested "X"-like shapes. The finite slopes of these dark bands show that the FQHE $R_{xx}$ minima shift in $B$ or $\nu$ with the $I_{DC}$. Figure 3b shows the color plot of Fig. 3a with overlaid solid, colored diagonal lines to indicate the evolution of the resistance minima with $|I_{DC}|$. In this plot 3(b), the dashed vertical lines mark the $\nu = p/q$ values for standard FQHE often observed over $2 \geq \nu \geq 1$. Note that the major vertices of these X's occur at $I_{DC} = 0$ μA at the $B$ corresponding to the 5/3, 8/5, 11/7, 14/9 and also the 4/3, 7/5, 10/7, 16/11, 9/7 FQHEs, which are some canonical FQHE in the span $2 \geq \nu \geq 1$. Thus, one might make the initial conjecture that a vertex is the signature of FQHE in such plots.

Figure 3c exhibits the overlaid lines from Fig. 3b without the color plot. Here, the green dots at the intersection of the positive- and negative-sloped lines at $I_{DC}$ = 0 signify the above-mentioned equilibrium FQHE. This plot shows, however, the possibility of vertices due to intersections between sloped lines at different, non-standard filling factors. For example, the negative sloped line originating at 4/3 intersects with the positive sloped line originating at 7/5 at a filling factor of 15/11 for $I_{DC} \approx \pm 0.6$ μA. Thus, this intersection or vertex has been marked as a light-red point in Fig. 3c. Analogously, other line intersections at finite $I_{DC}$ have been marked with light-red points in Fig. 3c. In Fig. 3d, these (now bright) red points have been overlaid on the color plot, now without the solid, sloping lines that appeared in Fig. 3b, c, in order to demonstrate that these special points are clearly visible, and, indeed, they are darker, in the bare color plot. In the next figure, some of these intersections are examined in greater detail.

Figure 4 exhibits three columns of plots. The same plot appears as Fig. 4a–c in the first row but each plot highlights a different span of $B$, which is marked with red vertical lines. In Fig. 4d, the yellow and the blue dots mark the equilibrium 4/3 and the 7/5 FQHE states, respectively, while the associated $R_{xx}$ and $R_{xy}$ traces are shown in Fig. 4j. The line traces in Fig. 4j confirm quantized plateaus in $R_{xy}$, which coincide with resistance minima in $R_{xx}$ at 4/3 and 7/5. Note that the vertical colored bars in yellow and blue coincide with the magnetic fields corresponding to the yellow and blue dots in Fig. 4d. As indicated by Fig. 4d, the noteworthy feature is that, with the application of the $|I_{DC}| \geq 0$, the 4/3 and the 7/5 states vanish, as their associated resistance minima shift with $B$ to give rise to a FQHE that emerges at 15/11, which is marked by the brown points. The line traces of $R_{xx}$ and $R_{xy}$ at finite bias current in the vicinity of $I_{DC}$ = 0.5 μA are shown in Fig. 4g. These line traces confirm that the Hall plateaus at 4/3 and 7/5 have vanished at these $I_{DC}$ as the Hall plateau develops and coincides with a local resistance minima in $R_{xx}$ at 15/11. Here, note that 15/11 − 11/11 = 4/11 is the most prominent expected FQHE between 1/3 and 2/5[36]. Figure 4e shows an expanded colored plot that highlights the bias-current dependence in the vicinity of the 7/5 (brown dot) and the 10/7 (green dot) states observable at $I_{DC}$ = 0. The line plots in Fig. 4k show the Hall plateau in $R_{xy}$ and the resistance minima in $R_{xx}$ in the vicinity of these states at $I_{DC}$ = 0, which are highlighted here by the brown and green vertical bands. Once again, a finite bias current, here $I_{DC} \approx 0.25$ μA, quenches the 7/5 and the 10/7 equilibrium FQHE states in favor of an even denominator plateau and resistance minimum near 17/12. Figure 4f shows an expanded colored plot that highlights the bias-current dependence in the vicinity of the 5/3 (blue dot) and the 8/5 (lime-green dot) states observable at $I_{DC}$ = 0. Associated line

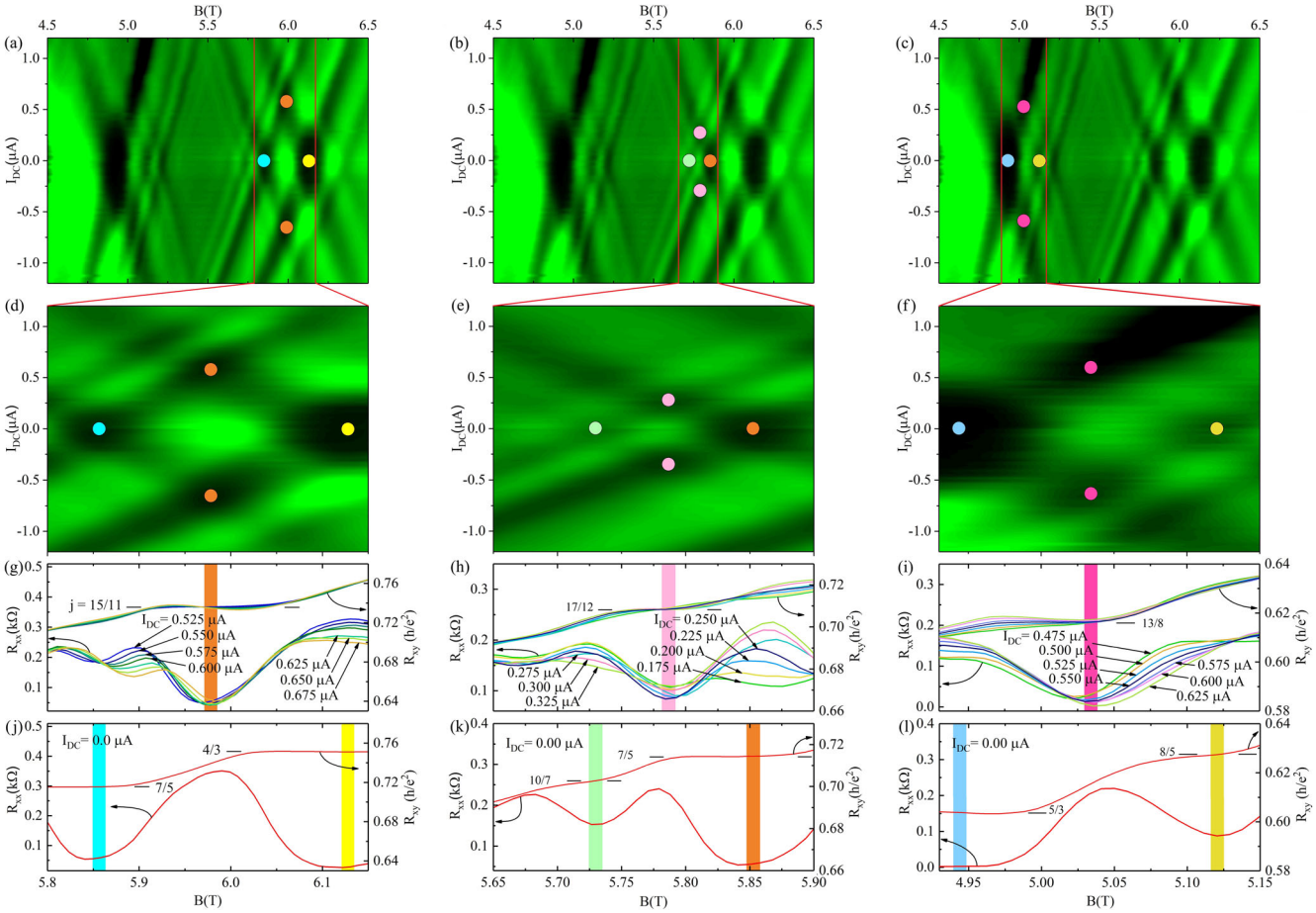


**Fig. 4 | Manifestation of non-equilibrium FQHE at branch line intersections.** The three columns examine the trajectory intersections that are marked by colored dots in panels (**a**–**c**), within the domain spanned by vertical lines. The second row with panels (**d**–**f**) shows a magnified image of the relevant part of the color plots of the diagonal resistance from the first row. In panels (**g**–**l**), $I_{DC}$ is the bias current, $R_{xx}$ is the diagonal resistance, and $R_{xy}$ is the off-diagonal Hall resistance. Panels (**g**–**i**), show line graphs of the $R_{xx}$, and $R_{xy}$ for $0.525 \le I_{DC} \le 0.675$ μA, $0.175 \le I_{DC} \le 0.325$ μA, and $0.475 \le I_{DC} \le 0.625$ μA, respectively. Panels (**g**–**i**) should be compared with panels (**j**–**l**), which show line graphs of $R_{xx}$ and $R_{xy}$ for $I_{DC} = 0$ μA. Fractionally quantized Hall effects in panels (**g**–**l**) are marked by short horizontal line segments. A comparision of the panel-pair (**j**, **g**) shows that the 4/3 and 7/5 FQHEs disappear in favor of 15/11. Similarly, the panel pair (**k**, **h**) shows that the 7/5 and 10/7 FQHEs disappear in favor of 17/12. Finally, the panel pair (**l**, **i**) shows that the 5/3 and 8/5 FQHEs disappear in favor of 13/8.

plots in Fig. 4l show the Hall plateau in $R_{xy}$ and the resistance minima in $R_{xx}$ in the vicinity of these states at $I_{DC} = 0$, which are highlighted here by the blue and lime-green bands. Once again, a finite bias current, here $I_{DC} \approx 0.55$ μA, quenches the 5/3 and the 8/5 equilibrium FQHE states in favor of a plateau and resistance minimum near 13/8. Note that $13/8 - 1 = 5/8$ could be a half-filling factor like state between $5/3 - 1 = 2/3$ and $8/5 - 1 = 3/5$[36].

Figure 5 compares $R_{xx}$ color plots obtained for three Hall bar sections with widths, $W = 400, 200, 100$ μm, in the sequential triple Hall bar device[37]. The panel Fig. 5a exhibits the color plot already examined in detail in this manuscript for the $W = 400$ μm wide Hall bar, while Fig. 5b shows the color plot for the 200 μm section, and Fig. 5c exhibits the color plot for the $W = 100$ μm Hall bar. The diagonal tracks of the resistance minima in the $I_{DC}$ vs. $B$ color plots of all three panels have been overlaid with positive and negative sloped lines to track the variation of the resistance minima with the bias current. Some correlations here are: (1) the similarity in the overall observed characteristics of the trajectories of the minima in all three Hall bars of different $W$, (2) the similar slopes (within experimental error) in the tilt of the overlaid lines, although the Hall bar width $W$ differs by up to a factor of four between Fig. 5a, c, (3) the disappearance of the equilibrium FQHE that occur with increasing bias current, $I_{DC}$, followed by (4) the formation of states at the line intersections at finite bias, as previously shown in Fig. 4. Here, the absence of a size dependence in the slope of these dotted lines is a noteworthy feature because, at a given $I_{DC}$, the Hall voltage $V_{xy}$ is the same in all three sections. But, due to the differing widths, the Hall electric field $E_H = V_{xy}/W$, differs substantially from section to section. The observed insensitivity in the slope to the device width suggests that this is not a Hall electric field-induced effect. Finally, (5) note that the color scale is roughly the same for all three panels, but the contrast is reduced with decreasing size. This suggests a reduced amplitude for the FQHE "Shubnikov -de Haas" oscillations in the resistance in the smaller specimens with reduced bulk scattering.

## Discussion

Fractional quantized Hall effects arise from the formation of a spectral/mobility gap or localized band at mostly odd-denominator rational fractional filling factors, which is manifested in vanishing diagonal resistance, and the formation of quantized Hall plateaus. These experiments show that the application of a bias current $I_{DC}$ produces a bimodal splitting of the resistance minima, with linear positively sloped and negatively sloped trajectories arising from each ($I_{DC} = 0$) equilibrium FQHE, in the $I_{DC}$ vs. $B$ color plots of the resistance (see Fig. 3). Further, when positively and negatively sloped tracks arising from different equilibrium FQHE intersect, the resistance minima become deeper and plateaus become manifested in the vicinity of these intersection points (Figs. 3–5). That is, the color plots show that the resistance minima trajectories form diamond-like patterns, with fractionally quantized Hall effects appearing also at the intersection of tracks originating from different equilibrium FQHE.

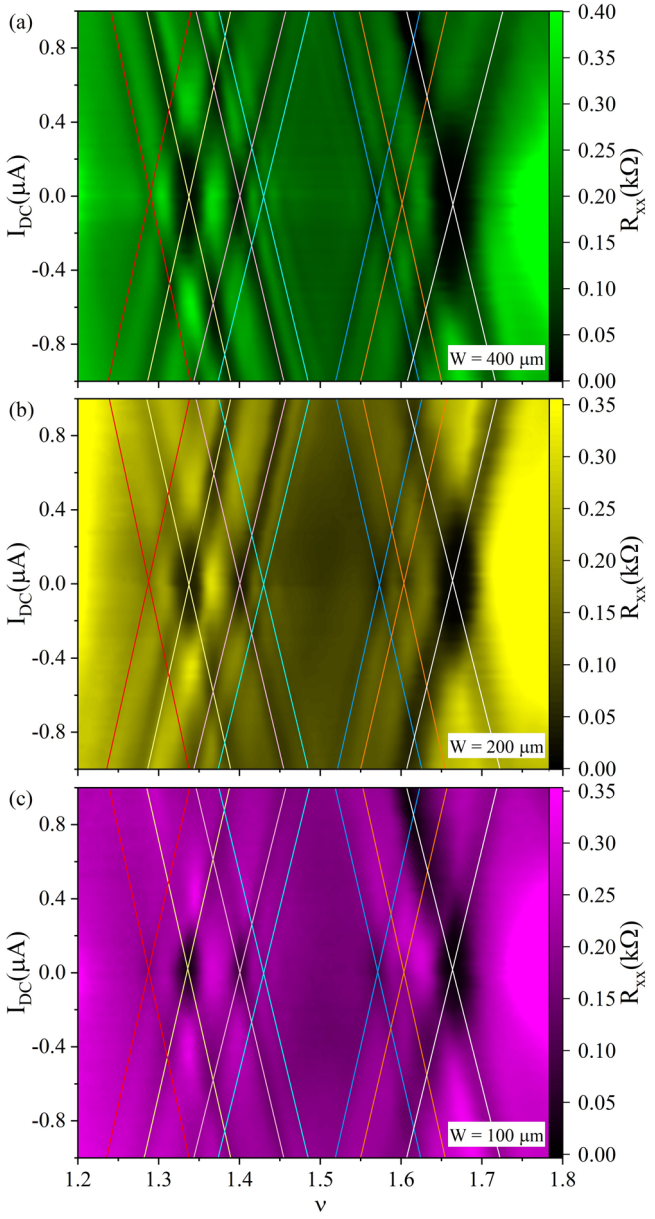


**Fig. 5 | Splitting of equilibrium FQHE states under current bias in Hall bars of different width, W.** The diagonal resistance $R_{xx}$ (color bar on the right) is plotted vs. the LL filling factor $\nu$ (abscissa) and $I_{DC}$ (ordinate). Solid colored lines trace the evolution of the $R_{xx}$ minima with $I_{DC}$. **a** Color plot of $R_{xx}$ for a Hall bar with width $W = 400$ μm. **b** Color plot of $R_{xx}$ for $W = 200$ μm. **c** Color plot of $R_{xx}$ for $W = 100$ μm. Refer to Fig. 2 for the definition of scale $W$. Note the similarly sloped lines for all $W$, although the contrast is reduced in the smaller specimen. Here, $T = 25$ mK.

The evolution of IQHEs and FQHEs with increasing current has been examined in studies of the so-called breakdown of the quantum Hall effect[41–45], which focused upon the disappearance of the IQHE, and FQHE, and its underlying causes in the high current limit. To our knowledge, such studies did not show a splitting of FQHE resistance minima with increasing current or the interaction of FQHE resistance minima originating at different canonical FQHE filling factors to give rise to new FQHE or consider the possibility of the reappearance of FQHE at a different filling factor—features that we have shown here. Thus, the phenomenology reported here looks different, in comparison to the usual breakdown phenomena[41].

We present a model here to help understand the observations. It recalls some aspects of the modeling for the diamond-like patterns observed in the color plots of the conductance as a function of $V_{D,S}$ (the drain-source voltage) and $V_G$ (the gate voltage) in electron charging experiments on small quantum dots[46], although charging is not involved here. Note that here, unlike in the quantum dot electron charging experiments, the characteristic device size, $W$, is very large and spans hundreds of micrometers in these specimens. Further, a gate potential is not applied in these experiments. However, it appears that the magnetic field plays the same role here as the gate voltage in the charging experiments: an increasing (decreasing) magnetic field serves to lower (raise) the filling factor of the underlying magnetic Landau levels, including mobility gaps/localized bands, just as the gate voltage serves to raise/lower the energy of the confined state in the charging experiments. Further, these experiments suggest that the applied $I_{DC}$ serves to create an internal bias similar to the source-drain bias in the charging experiments.

Figure 6 illustrates a model for the observation of two branches arising from one equilibrium FQHE state under finite current bias for the lowest Landau level (LL) case. In each illustration (a–j), from left to right, shown are the source (blue), a barrier, the LL (gray), a second barrier, and the drain (blue). The source and drain electrochemical potentials are $\mu_S$ and $\mu_D$, respectively. The LL-width is LLW, and the filling factor of the Landau level, shown in green, is $\nu$. As the magnetic field, $B$, increases from left to right, i.e., $B_0 \rightarrow B_4$, the Landau level degeneracy increases and, therefore, $\nu$ (the height of the green bar) decreases for a constant $n$, as indicated by the violet dotted line. The highest occupied state within the LL is marked as $E_F$. Orange denotes the mobility gap/localized band at a fractional filling $p/q$ of the Landau level. It is understood that this mobility gap for FQHE of a given filling factor occurs for a larger (smaller) carrier density at a higher (lower) magnetic field, $B$. (Experiment has also shown that, at a fixed magnetic field, increasing (decreasing) the carrier density helps to increase (decrease) the filling factor and thereby sweep through sequentially higher (lower) filling factor FQHE). Panels 6a, c, e, g, i and 6b, d, f, h, j consider coincidence at different dc bias currents ($I_{DC}$), for positive- and negative-bias current polarity, respectively, at different magnetic fields ($B$). Consider the equilibrium FQHE observed with $I_{DC} = 0$, which is shown in Fig. 6a, b: In this measurement configuration without a dc current bias, $I_{DC} = 0$, canonical FQHE is observed at $\nu = p/q$, where $E_F$ lies in the mobility gap (orange), and coincides with $\mu_S$ and $\mu_D$. The condition in Fig. 6a precludes carrier scattering within the 2DES and includes "forbidden entry" and "forbidden exit" (marked by red arrows with "x" in the figure) at $\mu_D$ and $\mu_S$, leading to vanishing $R_{xx}$ and $R_{xy} = (p/q)^{-1}(h/e^2)$ at, say, a magnetic field $B = B_2$. This situation is marked as a point at $I_{DC} = 0$, $B = B_2$ in Fig. 6k. Figure 6c illustrates the case where the filling factor is incrementally smaller due to increased LL degeneracy at the higher $B = B_3 > B_2$. Thus, the $E_F$ will fall below the mobility gap such that the top of the green bar lies below the orange band. However, with $I_{DC} = +I_0$, the finite bias between source and drain, shown here to be symmetric relative to $E_F$, helps to bring $\mu_D$ back into coincidence with the 'orange' mobility gap. This will produce an observable resistance minimum in the experiment because carrier entry at $\mu_D$ becomes forbidden. Figure 6d illustrates the case with $I_{DC} = -I_0$, i.e., current polarity reversal, where the localized band (orange) coincides now with $\mu_S$ at the higher magnetic field $B_3 > B_2$. Then, carrier entry is forbidden at $\mu_S$, and this again produces just a resistance minimum. Thus, at $B = B_3$, a resistance minimum associated with forbidden entry is observable at $I_{DC} = \pm I_0$, and these points are hence marked in Fig. 6k. At a lower magnetic field $B_1 < B_2$, where the filling factor is higher than at $B_2$, $E_F$ (top edge of the green band) rises above the mobility gap, see Fig. 6e. Yet, the $\mu_S$ can be brought into coincidence with the localized band with $I_{DC} = +I_0$. Then, carrier exit becomes forbidden so this produces a resistance minimum. With current bias reversal, i.e., $I_{DC} = -I_0$, see Fig. 6f, the localized band (orange) coincides with $\mu_D$ at a lower magnetic field $B_1 < B_2$. Carrier exit is again forbidden in this case, leading to a resistance minimum. Thus, at $B = B_1$, a resistance minimum associated with a forbidden exit is observable at $I_{DC} = \pm I_0$, and these points are also marked in Fig. 6k. The Fig. 6g, h cases are analogous to the Fig. 6c, d forbidden entry cases, respectively, with the difference that the bias currents are twice larger in magnitude, so the coincidence between the band of localized states and the drain/source occurs at the proportionately higher magnetic field $B_4$. The Fig. 6i, j cases are analogous to the Fig. 6e, f forbidden exit cases, respectively,

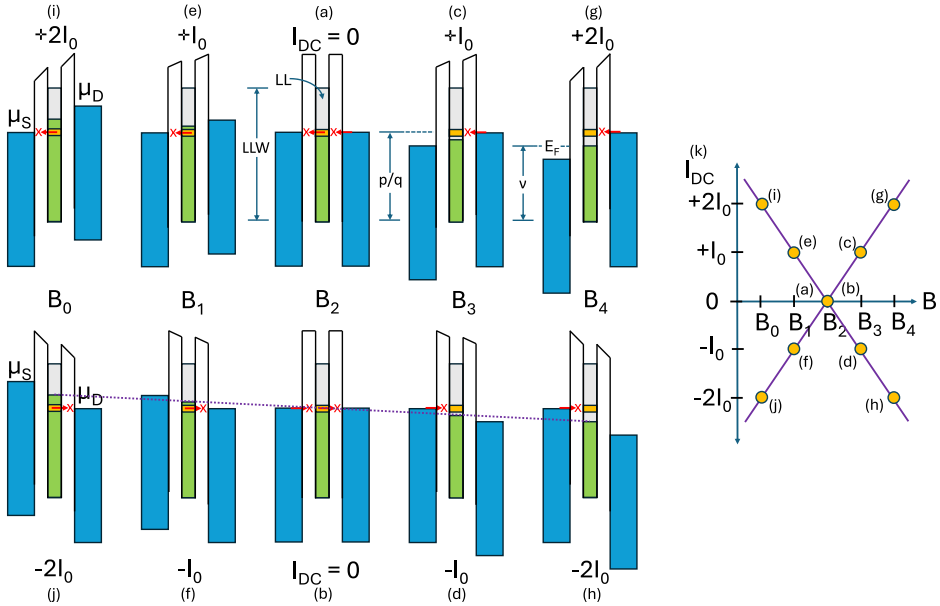


**Fig. 6 | Model for two resistance minima branches arising from one equilibrium FQHE state under current bias.** Illustrations (**a**–**j**) show the source (blue), a barrier, the Landau level (LL) (gray), a second barrier, and the drain (blue). The source and drain electrochemical potentials are $\mu_S$ and $\mu_D$, respectively. The LL-width is LLW. The highest occupied state is $E_F$. The LL-filling factor (green) is $\nu$. The violet dotted line shows $\nu$ decreasing with increasing magnetic field $B$. The orange band denotes a mobility gap/localized band at $\nu = p/q$. Panels (**a**, **c**, **e**, **g**, **i**) and (**b**, **d**, **f**, **h**, **j**) consider $\mu_S$ and/or $\mu_D$ coincidence with the mobility gap for positive and negative currents, respectively. **a**, **b** Canonical FQHE is observed at $\nu = p/q$ with $I_{DC} = 0$, where $E_F$ coincides with mobility gap, $\mu_S$, and $\mu_D$. This includes "forbidden entry" and "forbidden exit" (red arrows with "x") at $\mu_S$ and $\mu_D$. **c** At $B_3 > B_2$, the $E_F$ falls below the mobility gap. However, with $I_{DC} = +I_0$, the finite bias helps to bring $\mu_D$ back into coincidence with the mobility gap, which produces just an observable resistance minimum, as entry at $\mu_D$ becomes forbidden. **d** With $I_{DC} = -I_0$, the gap coincides now with $\mu_S$ at $B_3 > B_2$, then entry is forbidden, and this again produces a resistance minimum. **e** At $B_1 < B_2$, $E_F$ rises above the mobility gap. Yet, $\mu_S$ can coincide with the gap with $I_{DC} = +I_0$ and exit becomes forbidden. **f** With $I_{DC} = -I_0$, exit is again forbidden as the gap coincides with $\mu_D$. The (**g**) and (**h**) cases are analogous to the (**c**) and (**d**) forbidden entry cases, respectively, except the bias currents are twice larger in magnitude, so the coincidence occurs at $B_4 > B_2$. Similarly, the (**i**) and (**j**) cases are analogous to the (**e**) and (**f**) forbidden exit cases. **k** A $I_{DC}$ vs. $B$ plot conveys the results. Note the appearance of positively and negatively sloped lines for the resistance minima and their intersection at $I_{DC} = 0$, as in Fig. 3.

with the difference that the bias currents are twice larger in magnitude, so the coincidence between the band of localized states and the drain/source occurs at the proportionately lower magnetic field $B_0$. Note that the points included in Fig. 6k yield two lines, one with a positive and another with a negative slope, arising from the equilibrium FQHE, as observed in the experimental data shown in Fig. 3.

Figure 7 illustrates the model for the observed current bias-induced intersection of two branches arising from two equilibrium FQHE states, which leads to the observation of the non-equilibrium excited-state FQHEs in the experiment, as seen in Fig. 4g–i. Once again, in the figure panels, blue regions denote the source and drain, on the left and right, respectively, with chemical potentials $\mu_s$ and $\mu_d$. Orange and brown bands denote the mobility gaps at two distinct rational fractional fillings of the Landau level. Figure 7a, b show that at a fixed carrier density, with $I_{DC} = 0$, a canonical equilibrium ('orange') FQHE occurs at a magnetic field $B_2$, where $E_F$ lies in the orange mobility gap, and coincides with $\mu_S$ and $\mu_D$. Note the forbidden carrier entry and forbidden carrier exit in these cases. These cases are marked with an orange dot at $I_{DC} = 0$ and $B = B_2$ in Fig. 7k. At the higher magnetic field $B = B_6$, see Fig. 7c, d, another equilibrium ('brown') FQHE occurs when the brown mobility gap coincides, with $I_{DC} = 0$, with $\mu_S$ and $\mu_D$. These cases have been marked with a brown dot in Fig. 7k at $I_{DC} = 0$ and $B = B_6$. Note again the forbidden entry and forbidden exit here. As $B$ increases from $B_2$ to $B_6$, the Landau level filling $\nu$, i.e., the height of the green bar, decreases. In Fig. 7e, at a field $B_3 > B_2$, the filling factor drops below the orange mobility gap. However, an $I_{DC} = +I_0$ induced bias will serve to bring $\mu_D$ into coincidence with the orange mobility gap. Then, carrier entry at $\mu_D$ will be forbidden and a resistance minimum will become observable. Polarity reversal in the bias current, $I_{DC} = -I_0$, will serve to bring $\mu_S$ rather than $\mu_D$ into coincidence with the orange mobility gap, see Fig. 7f. Now, carrier entry at $\mu_S$ will be forbidden. Both Fig. 7e, f result in an observable resistance minimum at $B = B_3$ with $I_{DC} = \pm I_0$. At a field $B_5 < B_6$, the filling factor will have increased relative to that at $B_6$, such that $E_F$ (top of the green band) now lies above the brown mobility gap. However, an $I_{DC} = +I_0$ induced bias will serve to bring $\mu_S$ into coincidence with the brown localized band, see Fig. 7g. Then, carrier exit into the source will be forbidden. Here, polarity reversal in the bias current, $I_{DC} = -I_0$, see Fig. 7h, will serve to bring $\mu_D$ rather than $\mu_S$ into coincidence with the brown mobility gap. Now, carrier exit will again be forbidden. Both Fig. 7g, h result in an observable resistance minimum at $B = B_5$ with $I_{DC} = \pm I_0$, and these points are also marked in brown in Fig. 7k. Figure 7i, j exhibit the case at $B = B_4$, where the effective source-drain bias due to the applied $I_{DC}$ matches the energetic spacing of the orange and brown localized bands. In Fig. 7i, the $I_{DC} = +2I_0$ induced bias prevents carrier entry from the drain at $\mu_D$ due to the orange mobility gap and carrier exit at $\mu_S$ due to the brown mobility gap into the source. In Fig. 7j, the negative $I_{DC}$ prevents carrier entry from the source due to the orange mobility gap and carrier exit into the drain due to the brown mobility gap. Simply put, blocked entry and exit are realized here with the help of two different mobility gaps. Thus, a pair of half-orange/half-brown points appear in Fig. 7k at $B = B_4$ and $I = \pm 2I_0$. These illustrations suggest that while canonical FQHE includes blocked entry and exit due to a single mobility gap/localized band, blocked entry and exit due to two different localized bands working together, as in Fig. 7i, j, help to bring about non-equilibrium fractionally quantized Hall effects, especially if the sample size is comparable to or smaller than the inelastic or energy relaxation lengths, as could be the case in these experiments utilizing small specimens. Thus, the blocked entry and exit cases of Fig. 7i, j, at the finite $I_{DC}$ vertices of the diamond, apparently help to form the 15/11 in Fig. 4a or 13/8 in Fig. 4c at such current bias-induced intersection of two branches arising from two distinct equilibrium FQHE states.

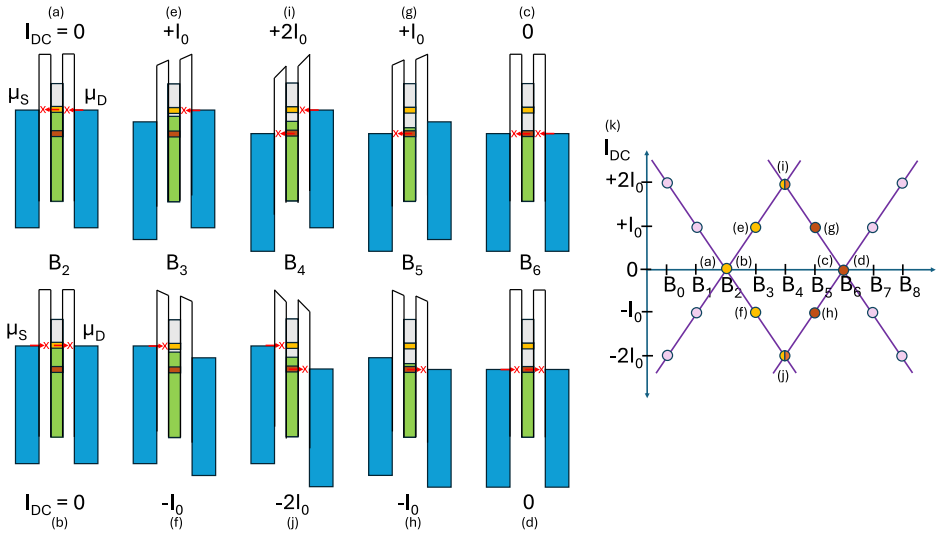


**Fig. 7 | Non-equilibrium excited-state FQHE occur at the intersection of branches arising from equilibrium FQHEs.** Each illustration (**a**–**j**) shows the source (blue), a barrier, the Landau level (LL) (gray), another barrier, and the drain (blue). The source (drain) electrochemical potential is $\mu_S$ ($\mu_D$). Orange and brown bands denote FQHE mobility gaps at two distinct LL fillings. **a**, **b** With $I_{DC} = 0$, an equilibrium (`orange') FQHE occurs at magnetic field $B = B_2$, where $E_F$ coincides with the orange gap, $\mu_S$, and $\mu_D$. Note the forbidden entry and forbidden exit at $\mu_S$ and $\mu_D$. **c**, **d** Similarly, with $I_{DC} = 0$, another equilibrium (`brown') FQHE occurs at $B = B_6$. **e** At $B_3 > B_2$, the LL filling (green bar) falls below the orange band. However, with $I_{DC} = +I_0$, $\mu_D$ comes into coincidence with the orange gap, and carrier entry at $\mu_D$ becomes forbidden. **f** $I_{DC} = -I_0$ brings $\mu_S$ into coincidence with the orange gap, and carrier entry at $\mu_S$ becomes forbidden. Thus, (**e**, **f**) indicate a resistance minimum at $B = B_3$. **g** At $B_5 < B_6$, the brown gap falls below the LL-Fermi level. However, $I_{DC} = +I_0$ serves to bring $\mu_S$ into coincidence with the brown gap, so that carrier exit becomes forbidden. **h** $I_{DC} = -I_0$ brings $\mu_D$ into coincidence with the brown gap. Both (**g**) and (**h**) result in a resistance minimum at $B = B_5$. **i**, **j** At $B = B_4$, the source-drain bias equals the spacing between the two mobility gaps. In (**i**), the orange gap prevents carrier entry at $\mu_D$, and the brown gap prevents carrier exit at $\mu_S$. In (**j**), carrier entry at $\mu_S$ and carrier exit at $\mu_D$ are forbidden. Thus, these two gaps work together to prevent carrier entry and exit, similar to the canonical FQHE cases (**a**, **b**) or (**c**, **d**). **k** A $I_{DC}$ vs. $B$ graph of the coincidence conditions exhibits the diamond shapes observed in Fig. 3. And, non-equilibrium, excited-state FQHEs, such as the 15/11 in Fig. 4g, occur at the diamond vertices. Orange (brown) dots signify coincidence between orange (brown) gap and $\mu_S$ and/or $\mu_D$. Orange-brown dots represent superposition. Magenta dots represent cases not examined.

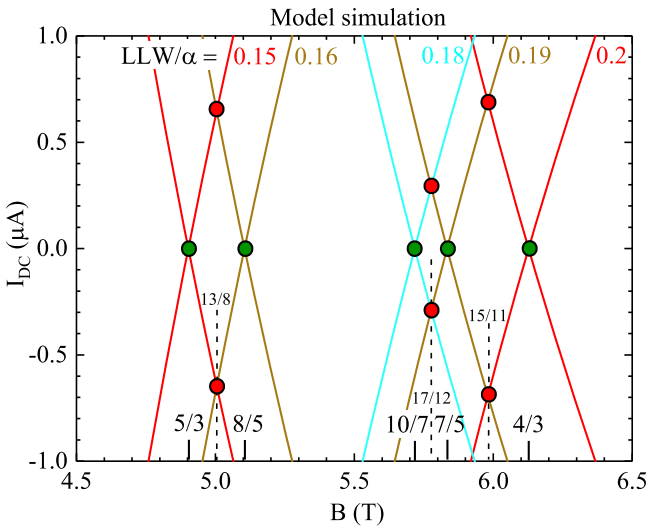


**Fig. 8 | Model simulation of the trajectories of the resistance minima in $I_{DC}$ vs. $B$.** The figure shows a fit of some trajectories of resistance minima seen in Fig. 3. The fitting parameter ratio $LLW/\alpha$ increases from $LLW/\alpha = 0.15$ for the 5/3 trajectories to $LLW/\alpha = 0.2$ for the 4/3 trajectories. In the figure, the green dots mark the canonical FQHE, and the red dots mark the observed non-equilibrium fractionally quantized Hall effects at finite $I_{DC}$ line intersections.

A simulation, see Fig. 8, based on the model of Figs. 6 and 7 is presented to complement the experimental results. For this simulation, the degeneracy of the LL has been distributed uniformly over the width LLW. If the electrochemical bias is given by $\Delta\mu = \mu_S - \mu_D = -\alpha e V_{xy} = -\alpha e I_{DC} B/ne$, where $\alpha$ is a proportionality constant, $n$ is the carrier density, $I_{DC}$ is the DC bias current, $B$ is the magnetic field, and $e$ is the electron charge, and if, as implied by the Fig. 6, half of this bias serves to line up the source or drain with a mobility gap, then $1/2(\mu_S - \mu_D) = -(1/2)\alpha e(I_{DC}B/ne) = \pm(\nu - \nu^*)LLW$, where $\nu^* = 4/3, 5/3, 8/5, 7/5, 10/7, \ldots$ is the filling factor for a canonical equilibrium FQHE, $\nu = nh/eB$, and $LLW$ is the LL broadening. From this, for $I_{DC}$ vs. $B$ about $\nu^*$, we obtain: $I_{DC} = \pm(LLW/\alpha)(2n/B)(nh/eB - \nu^*)$.

In Fig. 8, the simulated trajectories of the resistance minima are shown in an $I_{DC}$ vs. $B$ plot. For each pair of lines of the same color, the ratio of the free parameters $LLW$ and $\alpha$, i.e., $LLW/\alpha$, was adjusted to match the experimentally observed resistance minima trajectories (Fig. 3). In the model simulation, the green dots mark the canonical FQHE and the red dots mark the non-equilibrium FQHE at line intersections. The figure shows that $LLW/\alpha$ increases from $LLW/\alpha = 0.15$ for the 5/3 trajectories to $LLW/\alpha = 0.2$ for the 4/3 trajectories. At the moment, the experiment does not allow for a separate determination of $\alpha$ and $LLW$. From theory, it is understood that the electron-electron Coulomb energy, $E_C = e^2/(4\pi\epsilon_0\epsilon l_B) \approx 10$ meV, at $B = 5.5$ T, the center $B$-field value in Fig. 8, sets the scale of the Landau level broadening ($LLW$) due to interactions alone[47]. Here $l_B = (\hbar/eB)^{1/2}$, $\epsilon_0$ is the permittivity of free space, and $\epsilon$ is the dielectric constant for GaAs. Thus, it appears that the model of Figs. 6 and 7 helps to provide a qualitative understanding of the observations and a simulation of the minima trajectories, as per Fig. 8. The accurate extraction of the energy scales of interest such as the LL broadening (LLW), the energetic spacing between the mobility gaps associated with different canonical FQHE, or the width of the mobility gaps themselves calls, however, for a further "calibration" of scales in experiment, especially in the conversion of the $I_{DC}$ scale to the electrochemical potential bias, which will be the topic of further experiments.

In summary, we have shown that all observable canonical FQHE at $|I_{DC}| = 0$ between $2 \geq \nu \geq 1$ undergo bimodal linear splitting in the resistance minima vs. $I_{DC}$ for $|I_{DC}| > 0$, yielding diamond-like transport characteristics in the $I_{DC}$ vs. $B$ color plots of the resistance, as the equilibrium FQHE at 4/3, 7/5, 12/9, 5/3, 8/5, etc., are replaced with increasing $I_{DC}$ by (hybrid) non-equilibrium excited-state fractionally quantized Hall effects at the

intersection of the resistance minima branches originating from different equilibrium FQHE. Ongoing experiments also indicate the same diamond-like transport characteristics for FQHE with $\nu \leq 1$. It is worth noting that the modeling presented here suggests the existence of mobility gaps/localized bands associated with canonical FQHE, even at a very large deviation from the associated canonical rational fractional filling factors.

## Methods

GaAs/AlGaAs single heterojunctions with electron density $n = 2 \times 10^{11}$ cm$^{-2}$ and mobility $\mu = 19.5 \times 10^6$ cm$^{-2}$/Vs were patterned by photolithography into Hall bar type devices, including triple sequential Hall bars with width $W = 400$ μm, $W = 200$ μm, and $W = 100$ μm on the same chip[37,40,48–50]. The resulting devices were placed on chip carriers and loaded into dilution refrigerators with the specimen at the center of a superconducting solenoid magnet. Measurements were carried out both in a wet dilution refrigerator, with the specimen immersed in liquid, and in a dry dilution refrigerator, with the sample in vacuum. Identical results were observed in both cases. Magnetotransport measurements were performed using low-frequency lock-in techniques, with a supplementary *DC* bias current ($I_{DC}$), as indicated in the figures, applied to the specimen. The reported resistances are $R_{i,j} = V_{i,j}/I_{ac}$, where $V_{i,j}$ are the lock-in measured voltages at the low ac-current ($I_{ac}$) frequency. Data were examined at several $I_{ac}$ over the range $10 \leq I_{ac} \leq 50nA$. While the signal-to-noise ratio was improved at the higher $I_{ac}$, the characteristic features did not depend upon the ac-current. The length-to-width ratio associated with the measurement on each Hall bar section was $L/W = 1$.

## Data availability

Relevant data are available from the corresponding author upon reasonable request.

Received: 22 February 2024; Accepted: 27 July 2024;
Published online: 06 August 2024

## References

1. Prange, R. E. & Girvin, S. M. (eds) *The Quantum Hall Effect* 2nd edn (Springer, 1990).
2. Das Sarma, S. & Pinczuk, A. (eds) *Perspectives in Quantum Hall Effects* (Wiley, 1996).
3. Jain, J. K. *Composite Fermions* (Cambridge Univ. Press, 2007).
4. Goerbig, M. O. From the integer to the fractional quantum Hall effect in graphene. Preprint at *arXiv* https://doi.org/10.48550/arXiv.2207.03322 (2022).
5. Tsui, D. C., Stormer, H. L. & Gossaard, A. C. Two-dimensional magnetotransport in the extreme quantum limit. *Phys. Rev. Lett.* **48**, 1559–1562 (1982).
6. Pan, W., Baldwin, K. W., West, K. W., Pfeiffer, L. N. & Tsui, D. C. Fractional quantum Hall effect at Landau level filling $\nu = 4/11$. *Phys. Rev. B* **91**, 041301 (2015).
7. Laughlin, R. B. Anomalous quantum Hall effect: an incompressible quantum fluid with fractionally charged excitations. *Phys. Rev. Lett.* **50**, 1395–1398 (1983).
8. Bolotin, K. I., Ghahari, F., Shulman, M. D., Stormer, H. L. & Kim, P. Observation of fractional quantum Hall effect in graphene. *Nature* **462**, 196 (2009).
9. Dean, C. R. et al. Multicomponent fractional quantum Hall effect in graphene. *Nat. Phys.* **7**, 693–696 (2011).
10. Feldman, B. E. et al. Fractional quantum Hall phase transitions and four-flux composite fermions in graphene. *Phys. Rev. Lett.* **111**, 076802 (2013).
11. Amet, F. et al. Composite fermions and broken symmetries in graphene. *Nat. Commun.* **6**, 5838 (2015).
12. Liu, X. et al. Interlayer fractional quantum Hall effect in a coupled graphene double layer. *Nat. Phys.* **15**, 893–897 (2019).
13. Li, J. I. A. et al. Pairing states of composite fermions in double layer graphene. *Nat. Phys.* **15**, 898–903 (2019).
14. Cao, Y. et al. Tunable correlated states and spin-polarized phases in twisted bilayer-bilayer graphene. *Nature* **583**, 215–220 (2020).
15. Tsukazaki, A. et al. Observation of the fractional quantum Hall effect in an oxide. *Nat. Mater.* **9**, 889 (2010).
16. Maryenko, D., Falson, J., Kozuka, Y., Tsukazaki, A. & Kawasaki, M. Polarization dependent Landau level crossing in a two-dimensional electron system in a MgZnO/ZnO heterostructure. *Phys. Rev. B* **90**, 245303 (2014).
17. Falson, J. & Masashi, K. A review of the quantum Hall effects in MgZnO/ZnO heterostructures. *Rep. Prog. Phys.* **81**, 056501 (2018).
18. Cai, J. et al. Signatures of fractional quantum anomalous Hall states in twisted $MoTe_2$. *Nature* **622**, 63 (2023).
19. Park, H. et al. Observation of fractionally quantized anomalous Hall effect. *Nature* **622**, 74 (2023).
20. Furneaux, J. E. et al. Studies of the fractional quantum Hall effect in a silicon MOSFET. *Surf. Sci.* **170**, 154 (1986).
21. Kukushkin, I. V. & Timofeev, V. B. Fractional quantum Hall effect in silicon MOSFETs in *High Magnetic Fields in Semiconductor Physics*, *Springer Series in Solid-State Sciences*, Vol. 71 (ed. Landwehr, G.) (Springer, 1987).
22. Manfra, M. J. High mobility AlGaN/GaN heterostructures grown by plasma-assisted molecular beam epitaxy on semi-insulating GaN templates prepared by hydride vapor phase epitaxy. *J. Appl. Phys.* **92**, 338 (2002).
23. Mironov, O. A. et al. Fractional quantum Hall states in a Ge quantum well. *Phys. Rev. Lett.* **116**, 176802 (2016).
24. Ma, M. K. et al. Observation of fractional quantum Hall effect in an InAs quantum well. *Phys. Rev. B* **96**, 241301(R) (2017).
25. Tsukazaki, A. et al. Observation of the fractional quantum Hall effect in an oxide. *Nat. Mater.* **9**, 889–893 (2010).
26. Falson, J. et al. Even-denominator fractional quantum Hall physics in ZnO. *Nat. Phys.* **11**, 347–351 (2015).
27. Ki, D.-K., Falko, V. I., Albanin, D. A. & Morpurgo, A. F. Observation of even denominator fractional quantum Hall effect in suspended bilayer graphene. *Nano Lett.* **14**, 2135 (2014).
28. Yang, J. et al. Integer and fractional quantum Hall effect in ultrahigh quality few-layer black phosphorus transistors. *Nano Lett.* **18**, 229 (2018).
29. Zhao, S. et al. Probing the fractional quantum Hall phases in valley-layer locked bilayer $MoS_2$. Preprint at *arXiv* https://doi.org/10.48550/arXiv.2308.02821 (2023).
30. Shi, Q. et al. Odd- and even denominator fractional quantum Hall states in monolayer $WSe_2$. *Nat. Nanotechnol.* **15**, 569 (2020).
31. Mani, R. G. et al. Zero-resistance states induced by electromagnetic-wave excitation in GaAs/AlGaAs devices. *Nature* **420**, 646–649 (2002).
32. Yang, B. & Balram, A. C. Elementary excitations in fractional quantum Hall effect from classical constraints. *New J. Phys.* **23**, 013001 (2021).
33. Eckel, J. et al. Comparative study of theoretical methods for non-equilibrium quantum transport. *New J. Phys.* **12**, 043042 (2010).
34. Halperin, B. I., Lee, P. A. & Read, N. Theory of the half-filled Landau level. *Phys. Rev. B* **47**, 7312 (1993).
35. Du, R. R. et al. Fractional quantum Hall effect around $\nu = 3/2$: composite fermions with a spin. *Phys. Rev. Lett* **75**, 3926 (1995).
36. Mani, R. G. & Klitzing, K. V. Fractional quantum Hall effects as an example of fractal geometry in nature. *Z. Phys. B* **100**, 635–642 (1996).
37. Mani, R. G., Kriisa, A. & Wegscheider, W. Size-dependent giant magnetoresistance in millimeter scale GaAs/AlGaAs 2D electron devices. *Sci. Rep.* **3**, 2747 (2013).
38. Mani, R. G. et al. Marginal metallic state at a fractional filling of '8/5' and '4/3' of Landau levels in the GaAs/AlGaAs 2D electron system. *Sci. Rep.* **11**, 15003 (2021).
39. Wijewardena, U. K. et al. Size dependence- and induced transformations- of fractional quantum Hall effects under tilted magnetic fields. *Sci Rep* **12**, 19204 (2022).

40. Mani, R. G. Dual ordinary, integral quantum, and fractional quantum Hall effects in partially gated doubly connected GaAs/AlGaAs heterostructure devices. *Phys. Rev. B* **55**, 15838 (1997).
41. Nachtwei, G. Breakdown of the quantum Hall effect. *Phys. E* **4**, 79 (1999).
42. Mani, R. G. & Anderson, J. R. Inhomogeneous broadening and the breakdown of the quantum Hall effect in GaAs/AlGaAs devices. *Sol. St. Commun.* **72**, 949 (1989).
43. Tsemekhman, V. et al. Theory of the breakdown of the quantum Hall effect. *Phys. Rev. B* **55**, R10201(R) (1997).
44. Watts, J. P. et al. Current breakdown of the fractional quantum Hall effect through contactless detection of induced currents. *Phys. Rev. Lett.* **81**, 4220–4223 (1998).
45. Dillard, C., Lin, X., Kastner, M. A., Pfeiffer, L. N. & West, K. W. Breakdown of the integer and fractional quantum Hall states in a quantum point contact. *Phys. E: Low-Dimens. Syst. Nanostructures* **47**, 290–296 (2013).
46. Kouwenhoven, L. P., Austing, D. G. & Tarucha, S. Few-electron quantum dots. *Rep. Prog. Phys.* **64**, 701 (2001).
47. Tong, D. Lectures on the quantum Hall effect. Preprint at *arXiv* https://doi.org/10.48550/arXiv.1606.06687 (2016).
48. Mani, R. G. Dual simultaneous Hall effects in inhomogeneous doubly connected GaAs/AlGaAs heterostructure devices. *Appl. Phys. Lett.* **70**, 2879 (1997).
49. Mani, R. G. Experimental technique for realizing dual and multiple Hall effects in a single specimen. *Europhys. Lett.* **34**, 139 (1996).
50. Mani, R. G. Transport study of GaAs/AlGaAs heterostructures and n-type GaAs devices in the “anti Hall bar within a Hall bar” configuration. *J. Phys. Soc. Jpn.* **65**, 1751 (1996).


## Acknowledgements

This work was supported at Georgia State University by the NSF under ECCS 1710302 and DMR 2210180, and the Army Research Office under W911NF-15-1-0433, W911NF-21-1-0285, and W911NF-23-1-0203. Thanks to R. Samaraweera, T. R. Nanayakkara and R. Poudel for technical assistance.

## Author contributions

Magnetotransport measurements by U.K.W. Experimental concept and data modeling by R.G.M. and U.K.W. Samples by A.K., U.K.W., and R.G.M. Manuscript by R.G.M. and U.K.W. High-quality MBE grown wafers by C.R. and W.W.

## Competing interests

The authors declare no competing interests.

## Additional information

**Correspondence** and requests for materials should be addressed to Ramesh G. Mani.

**Peer review information** *Communications Physics* thanks Jesús Iñarrea, James Nakamura and the other anonymous reviewer(s) for their contribution to the peer review of this work.